

Evaluation of quasi-static indentation response of superelastic shape memory alloy embedded GFRP laminates using AE monitoring

Luv Verma^a, J. Jefferson Andrew^{a,b}, Srinivasan M. Sivakumar^a, G. Balaganesan^c, S. Vedantam^d, Hom N. Dhakal^{e,*}

^a Department of Applied Mechanics, IIT Madras, Chennai, 600036, India

^b Department of Mechanical Engineering, Khalifa University of Science and Technology, Masdar Campus, Masdar City, P.O. Box 54224, Abu Dhabi, United Arab Emirates

^c Department of Mechanical Engineering, IIT Jammu, J&K, 181 221, India

^d Department of Engineering Design, IIT Madras, Chennai, 600036, India

^e School of Mechanical and Design Engineering, University of Portsmouth, Anglesea Road, Anglesea Building, PO1 3DJ, UK

ARTICLE INFO

Keywords:

Superelastic shape memory alloy (SE-SMA)
wires
Quasi-static indentation
GFRP
Glass/epoxy composite materials
Acoustic emission (AE) monitoring
Damage mechanisms

ABSTRACT

In this paper, the potential of superelastic shape memory alloy (SE-SMA) wire embedded architectures to increase the quasi-static indentation properties of a laminated glass/epoxy composite material was evaluated. Three types of SE-SMA configurations namely straight independent, meshed and anchored wires were embedded in the glass/epoxy composite laminates via a vacuum bag resin infusion technique. Throughout this investigation, the changes in the quasi-static indentation behavior and allied damage mechanisms due to these embeddings were compared with the homogenous glass/epoxy laminates. Real time acoustic emission (AE) monitoring technique was employed to characterize the damage profile of the different glass/epoxy specimens during the quasi-static indentation tests. The experimental results showed that SE-SMA embedments play a vital role in increasing the penetration resistance by enhancing redistribution of the indentation load all across the laminates. In particular, the meshed specimens restricted penetration of an indenter and delayed the critical fiber fracture unlike homogeneous and straight wired ones, whereas the anchored specimens further restricted extensive SMA/matrix pull-out, unlike meshed ones and provided the most excellent balance among rigidity, rear face fiber breakage, and SMA/matrix pull-out. Straight, meshed and anchored SE-SMA wires increased the load-carrying capacity approximately by 31%, 79%, and 100%, respectively, in comparison to the homogeneous ones.

1. Introduction

Conventional composite laminates are playing a vital role in different industries such as aerospace, marine, and automobile due to their high strength to weight and stiffness to weight ratios. Though, excellent in loading along fiber direction, composites suffer from poor indentation and impact response under transverse loading which is a crucial parameter in designing structural applications. For instance, tool drops, bird strikes, and wind loads on different aircraft structures such as radar antenna, fuselage, wings nacelle, and propeller blades, create internal damage in the composites and affect their strength [1,2]. Under transverse loads, failure initiates in the form of matrix cracking and as load increases, matrix cracking progresses as delamination which further leads to fiber failure and perforation of composites [3–5].

As the name implies, the shape memory alloys (SMAs) have ability to recover shapes while still maintaining significant amount of recovery stress. One of the promising ways to increase the energy absorption in composites is to incorporate highly ductile secondary reinforcements in addition to primary reinforcements [6,7]. Many researchers have used superelastic shape memory alloys (SE-SMA) as secondary reinforcement in composites to improve their response under transverse loads [8,9]. SE-SMA can undergo a high amount of strain which can lead to an increase in energy absorption [10,11]. Common metals such as aluminum and steel absorb all of their energy through plastic deformation. In addition to plastic deformation, there is a large plateau region in the SE-SMA stress-strain curve known as phase transformation which leads to a large amount of strain energy absorption in comparison to the common metals [12]. Due to phase transformation, SE-SMA (Nitinol) is

* Corresponding author.

E-mail address: hom.dhakal@port.ac.uk (H.N. Dhakal).

<https://doi.org/10.1016/j.polymertesting.2020.106942>

Received 23 July 2020; Received in revised form 15 October 2020; Accepted 30 October 2020

Available online 7 November 2020

0142-9418/© 2020 The Authors.

Published by Elsevier Ltd.

This is an open access article under the CC BY-NC-ND license

(<http://creativecommons.org/licenses/by-nd/4.0/>).

capable of withstanding ultimate stresses more than 1400–1700 MPa and can undergo around 8% of recoverable strain and 20% of ultimate strain [13,14]. Due to their high ultimate strength and strain dissipation properties, SE-SMA (Nitinol) dissipates strain energy four times more than any high alloy steel and sixteen times more than the graphite/epoxy composite [12,15,16]. The density of SE-SMA (6.45 g/cm^3) is also less than steel ($7.75\text{--}8.05 \text{ g/cm}^3$). Besides high strength, SE-SMA has numerous advantages over steel such as they are non-magnetic, high corrosion resistance, and reduced footprint [16,17]. They were also employed in the past to avoid the problem of fracture and transverse cracks between the carbon fiber and matrix, and improve the reliability of aircraft structures. SE-SMA cables are also employed in construction and mechanical industries against extreme loads (e.g. seismic applications) [18,19]. From the investigations presented above, it can be said that employing SE-SMA (Nitinol) over the metallic wires as secondary reinforcements can improve the indentation response and further increase the impact resistance of composites under transverse loads [20].

Though SE-SMA absorbs a high amount of energy, it is important to look at the interfacial bonding properties between SE-SMA and matrix as bonding affects the load transfer between the two and in turn affects the distribution of transverse load through the SE-SMA. To improve their bonding, researchers have employed the surface treatment methods such as chemicals to produce a porous oxide layer (improving wetting properties), and sandblasting [21,22]. Though they increase the bond strength, once debonding between SE-SMA and matrix initiates, interfacial strength weakens. This further leads to the propagation of debonding along the embedded length of SE-SMA limiting the energy absorption [23]. As the load is increased further, penetration of an impactor through the composite leads to SMA pull-out.

In the past, dynamic impact loads were commonly employed to assess the transverse mechanical responses [24–27]. However, under transient impact loads, the progression of damage events is complex to be characterized and only the ultimate damage state is observable after an impact event. It is normally agreed in the previous literature that quasi-static indentation load and low-velocity impact load lead to identical damage mechanisms [27–31]. Thus, many authors have employed multiple quasi-static indentation tests for monitoring of damage mechanism through interrupted cyclic indentation tests, conducted in parallel with non-destructive monitoring [32,33] and destructively after the application of mechanical load on separate specimens [34]. Indentation damages can also be produced by in-service events (careless handling) or interaction with the connected structures such as pillars, bends, etc. [35]. Hence, it is of great realistic importance to characterize the quasi-static indentation response of SE-SMA based composites. Non-destructive techniques (NDT) such as acoustic emission (AE) monitoring, digital image correlation (DIC), shearography, and thermography are frequently used on composites to characterize the damage progression [36–38]. Due to ease of real-time monitoring of dynamic changes (i.e. failure progression) within an anisotropic composite laminate, AE monitoring has garnered significant attention in recent times [39–41]. Damage modes characterization can be done based on the frequency content of the AE event, which in turn can be measured using Fast Fourier Transform (FFT). Though many researchers have worked to characterize the composite behavior in the multiple indentation regimes using AE monitoring [42–45], limited investigations have been done on the response of SE-SMA embedded composites.

In the present work, the quasi-static indentation response of the SE-SMA embedded GFRP composite laminates is investigated using AE monitoring. The innovation done in this work is the novel SE-SMA embedment configuration which is used as a secondary reinforcement in the glass-epoxy composite specimens. To evaluate and compare the indentation response of composite specimens embedded with SE-SMA, four different types of specimens have been considered for investigation. Type I specimens are the homogenous GFRP composite. Type II specimens are the GFRPs embedded with SE-SMA as straight wire

Table 1
Material properties of SE-SMA.

S. No.	Properties	Values (SE-SMA)	Units
1	E_{aus}	80	GPa
2	E_{mar}	40	GPa
3	Poisson's ratio	0.3	—
4	Density	6800	$\text{kg}\cdot\text{m}^{-3}$
5	Yield stress	800	MPa

Table 2
Material properties of glass-fiber.

S. No.	Properties	Values (SE-SMA)	Units
1	Young's modulus	76.6	GPa
2	Specific gravity	2.5	—
3	Specific modulus	0.0340	$\text{GPa}\cdot\text{m}^3/\text{kg}$
4	Specific strength	0.6200	$\text{MPa}\cdot\text{m}^3/\text{kg}$
5	Poisson's ratio	0.25	—

Table 3
Material properties of epoxy.

S. No.	Properties	Values	Units
1	Specific gravity	1.28	—
2	Young's modulus	3.792	GPa
3	Poisson's ratio	0.30	—

(conventional) without any restrainers. Type III specimens are the GFRP embedded with SE-SMA bi-directional mesh. Type IV specimens are the GFRP embedded with SE-SMA running in direction 1 and have been anchored (novel) with another SE-SMA wire (at regular intervals) running in direction 2. Direction 1 and 2 are orthogonal to each other. Parameters such as ultimate load, stiffness, and residual deformation are investigated for assessing the mechanical performance of SE-SMA embedded composites.

2. Experimental procedure

2.1. Materials and fabrication

Bidirectional woven roving mat (WRM) of glass fiber having areal density 360 g/m^2 was used as the primary reinforcement for composite laminates. Superelastic SMA wire (Nitinol: Nickel–Titanium Alloy i.e. 50 at % of NiTi) was used as a secondary reinforcement. As our aim was to exploit the energy absorption capabilities of SMA wire until it either reached plastic deformation or failure, no training was applied. Epoxy resin (LY 556) and hardener (HY951) were used in the weight ratio of 10:1 [45]. The properties of various materials employed to fabricate the specimens are given in Tables 1–3 and S1. Six layered glass/epoxy specimens were fabricated using a vacuum-assisted resin infusion process at a curing temperature of 30°C under a maintained vacuum gauge pressure of 30 mm Hg for 24 h. ASTM D6264-98(04) standard indentation specimens of dimension $150 \times 100 \text{ mm}$ were machined from the parent laminates using an abrasive waterjet cutting machine.

Four types of specimens were prepared to test as shown in Fig. 1. In the first type, specimens were fabricated using only glass fiber and epoxy matrix. In the second type, four SE-SMA wires of length 70 mm were used in between the 3rd and 4th GFRP layers as an embedment. In the third type, a mesh of SE-SMA wire was used between the 3rd and 4th GFRP layers. In direction 1, (D-1) wires of length 70 mm were laid, then they were meshed by SE-SMA wire from direction 2 (D-2). Similarly, in the fourth type, SE-SMA in direction 1 (D-1) was anchored with SE-SMA in direction 2 (D-2) by tying knots and placed in between the 3rd and 4th GFRP layers (Fig. S3). Respective volume fractions of the SMA content in the straight wired, meshed and anchored configurations were 2.10, 4.84

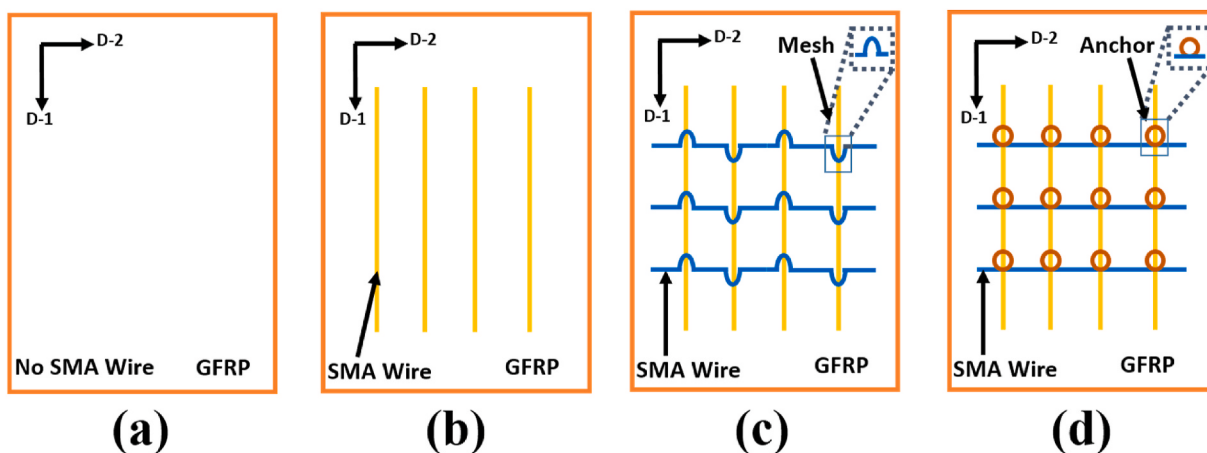


Fig. 1. Top-view schematics of different specimen configurations tested: (a) Type I, (b) Type II, (c) Type III and (d) Type IV specimens.

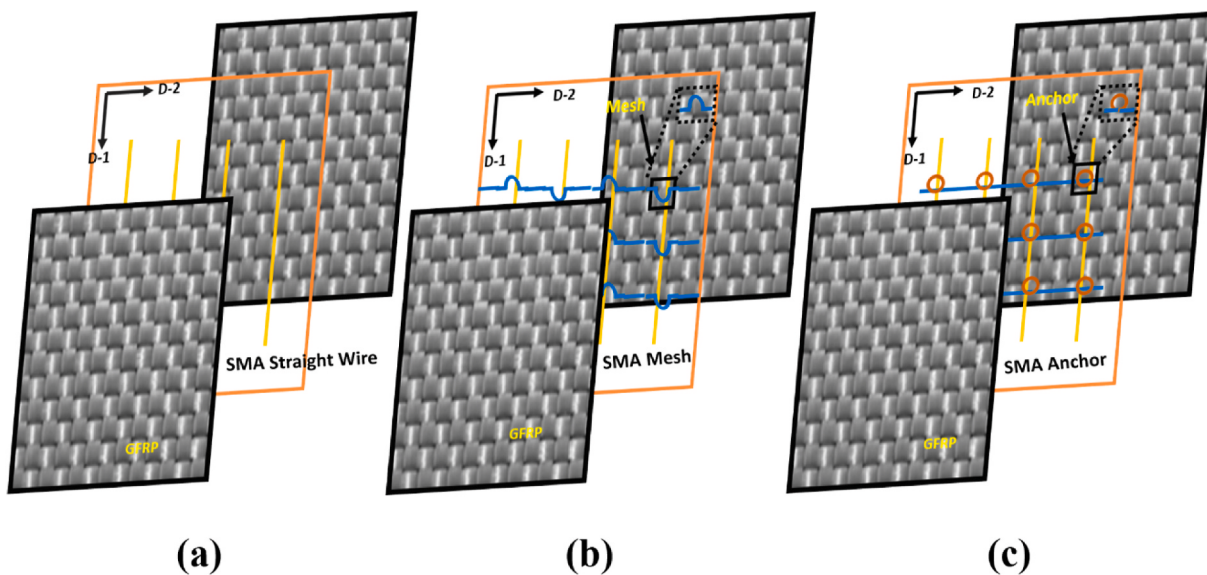


Fig. 2. The structure of SE-SMA based composite specimens considered in this study: (a) Type II, (b) Type III and (c) Type IV specimens.

Table 4
Code for different glass/epoxy specimens.

S. No.	Specimen	Connection type	Nomenclature
1.	Glass/epoxy (GFRP)	–	Type I
2.	Independent SMA straight wires embedding in GFRP	Independent	Type II
3.	Meshed SMA embedding in GFRP	Mesh points	Type III
4.	Anchored SMA embedding in GFRP	Knot points	Type IV

and 5.21%. Fig. 2 shows the structure of SE-SMA composite specimens considered in this study. The diameter of the SE-SMA wire used was 0.3 mm. The nominal distance between the wires in both directions was maintained to be 6 mm, which was considered to be less than the indenter's diameter 12.7 mm. The overall thickness of the specimens of all the configuration was maintained the same (3.15 ± 0.2 mm). The composite laminates were fabricated using six layers of the glass fibers to maintain the overall thickness of the specimens well in the range of the ASTM standard. The code for different glass/epoxy specimens is summed up in Table 4.

2.2. Quasi-static indentation (QSI) tests

Quasi-static cyclic indentation tests were performed as per ASTM D6264-98(04) using a 100 kN Tinus Olsen Universal Testing Machine (UTM). Four corners were clamped tightly with the help of toggle clamps as shown in Fig. 3. Cyclic indentation tests were performed via incremental displacement step control. From the incipient contact point, the displacement steps namely 2, 4, 6, 8, 10, and 12 mm were applied consecutively. The feed rate was set as 1 mm/min. For each type of specimen, five tests were performed and average results were considered to calculate ultimate load, stiffness and residual deformation.

2.3. Acoustic emission (AE) monitoring

Acoustic emission (AE) system, supplied by Physical Acoustic Corporation (PAC), was particularly used for damage monitoring while the sample underwent quasi-static multiple indentation tests. The device had 8 channels and samples the data at the rate of 3 MHz with 40 dB pre-amplification. During the test, AE monitoring was done by bonding two wide bands (WD) sensors in a linear arrangement over the specimen surface using high vacuum silicon grease. The distance between these two sensors was maintained to be 100 mm. The threshold of 45 dB was

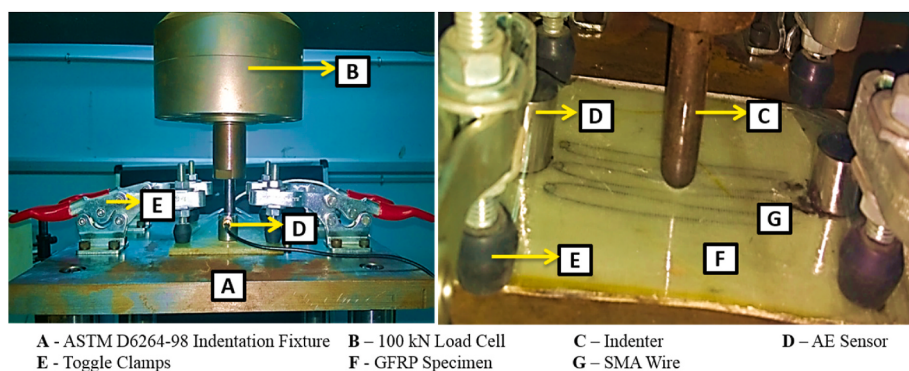


Fig. 3. SE-SMA based glass/epoxy specimen clamped in ASTM D 6264-98 indentation fixture.

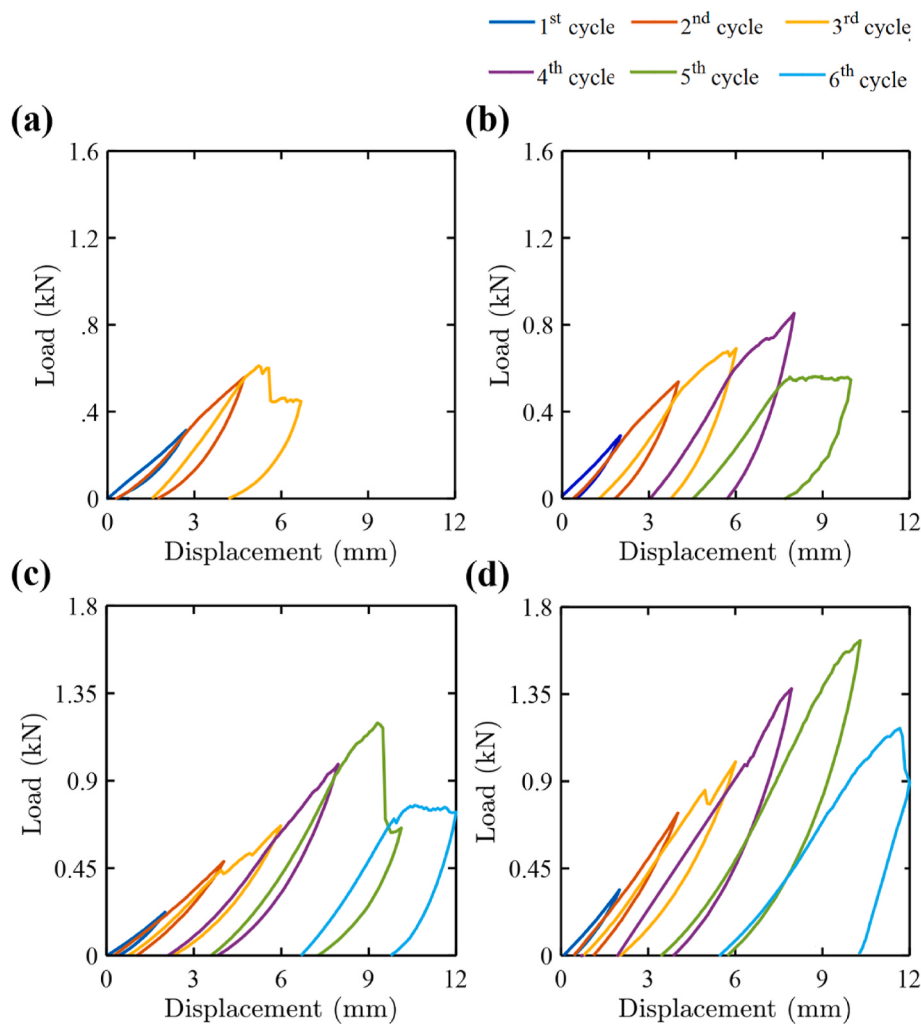


Fig. 4. Load-displacement curves for (a) Type I (Neat), (b) Type II (Straight), (c) Type III (Meshed) and (d) Type IV (Anchored) specimens.

used to filter ambient noise. Hsu-Nielson pencil lead break test was conducted to estimate the wave velocity of the samples. The average wave velocities in the configurations were 3146.3 m/s. The signal definition time used for AE monitoring was as follows: Peak Definition Time (PDT) is 28.57 μ s, Hit Definition Time (HDT) is 428.57 μ s, and Hit Lock-Out Time (HLOT) is 160 μ s?

3. Results and discussion

3.1. Cyclic indentation test

Cyclic quasi-static indentation tests coupled with AE monitoring were performed to study the indentation response of various SE-SMA based composite specimens. The indentation response of each specimen was recorded in terms of load vs. displacement curves and the key indentation parameters like ultimate load, stiffness and residual

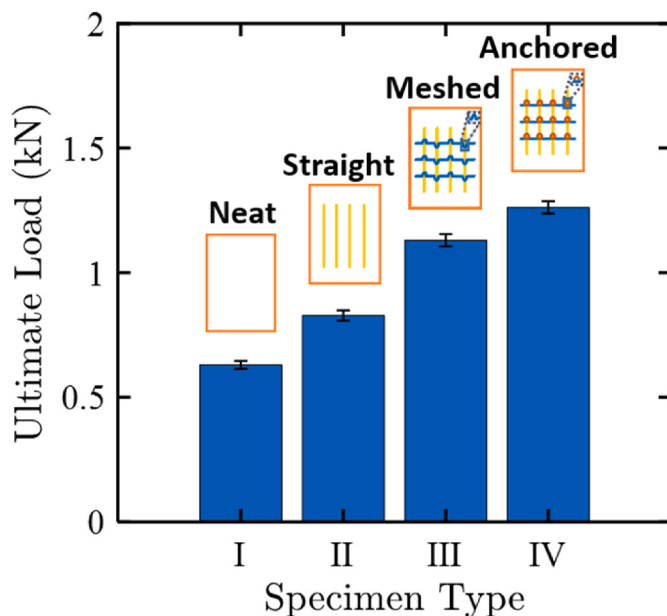


Fig. 5. Ultimate load of different glass/epoxy specimens.

Table 5
Maximum cycles to failure and ultimate displacement properties of different glass/epoxy specimens.

Specimens	Maximum cycles to failure	Ultimate displacement (mm)
Type I	3	4.93
Type II	4	8.00
Type III	5	9.31
Type IV	5	10.00

deformation were considered for assessing the performance of different specimens.

Fig. 4 depicts the load-displacement curves of different glass/epoxy specimens. Following the experimental curves, the ultimate indentation load of various glass/epoxy specimens is illustrated in Fig. 5. The maximum number of cycles to failure and ultimate displacement properties are listed in Table 5. It can be observed that the cyclic indentation behavior varied substantially with the architecture of SE-SMA wire. From Fig. 5, the Type IV specimens have the highest load-carrying capability, whereas Type I specimens have the least. In particular, embedding glass/epoxy specimens using Type II, Type III and Type IV

SMA wires increased the ultimate indentation load by 31.42%, 79.36%, and 100.31%, respectively, in comparison to Type I specimens. To understand the reason for these observations, stiffness progression, permanent deflection progression, and AE signatures of various glass/epoxy specimens under cyclic indentation tests are correlated and explained in the following sections.

3.2. Frequency analysis of AE signals

Before correlating the cyclic indentation test results with AE signatures, the damage mode allied with different recorded AE events were identified using peak frequency analysis. In the peak frequency analysis, the AE energy allied with various damage mechanisms is associated with the value of strain energy released. As a result, each AE event has a unique character, in the sense that its peak frequency is allied with the failure modes [42], such as resin cracking, fiber/matrix debonding, SMA/matrix debonding and fiber fracture. Though the frequency ranges for fiber/matrix damage modes are well established, it is important to identify the ranges of frequency in which SE-SMA/matrix failure modes are dominant. The peak frequency vs. time plot for glass/epoxy and SE-SMA based glass/epoxy specimens subjected to indentation tests are depicted in Fig. 6. Three distinct ranges (R1, R2, and R3) of peak frequencies were observed for glass/epoxy specimens, while, for SE-SMA based specimens, four ranges (R1, R2, R3, and R4) were observed. To identify the AE events allied with the different failure mechanisms, standard specimens such as homogeneous neat epoxy, particulate glass fiber reinforced epoxy, continuous glass fiber reinforced epoxy, and SE-SMA/epoxy specimens were used.

The neat epoxy specimens were subjected to an indentation test with AE monitoring to identify AE events allied with matrix cracking. Fig. 7 (a) depicts the FFT magnitude allied with the resin cracking signal acquired from the neat epoxy specimen. From the FFT magnitude plot, the frequency content of the resin cracking was recorded in the range of 60–140 kHz, with numerous AE events between 90 and 100 kHz, as proposed by Refs. [43,44]. From this analysis, it can be noticed that most of the AE events under range R1 (Fig. 6 (a)) have closely similar frequency values as that of homogeneous neat epoxy standard specimens. Hence, the range R1 is evidently associated with matrix or resin cracking. A typical matrix cracking on the neat epoxy specimen, as described by SEM, is depicted in Fig. 8 (a).

Fiber/matrix debonding AE events were identified from particulate glass fiber reinforced epoxy specimens. It is suggested that the possible damage modes allied with particulate glass fiber reinforced epoxy specimens are resin cracking and fiber/matrix debonding [41]. Two dominant frequent contents were acquired, namely 60–140 kHz and 210–270 kHz. From the results of neat epoxy specimens, the AE events

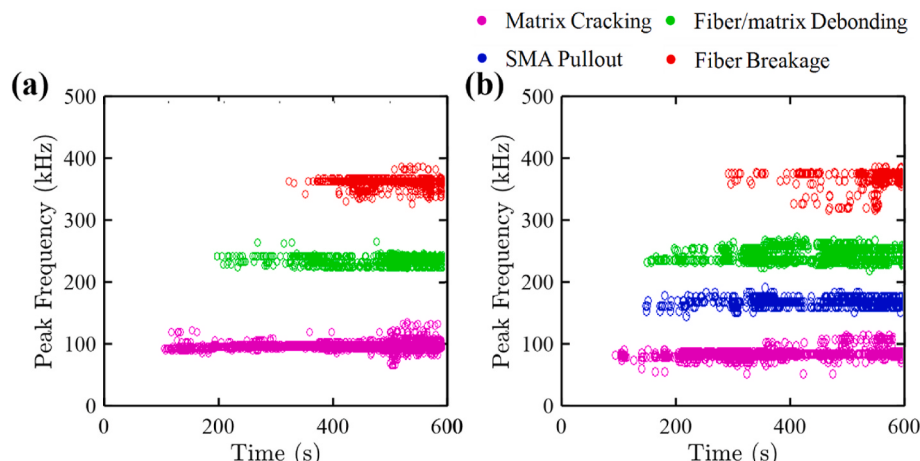


Fig. 6. Peak frequency vs. time plot for (a) glass/epoxy and (b) SE-SMA based glass/epoxy specimens.

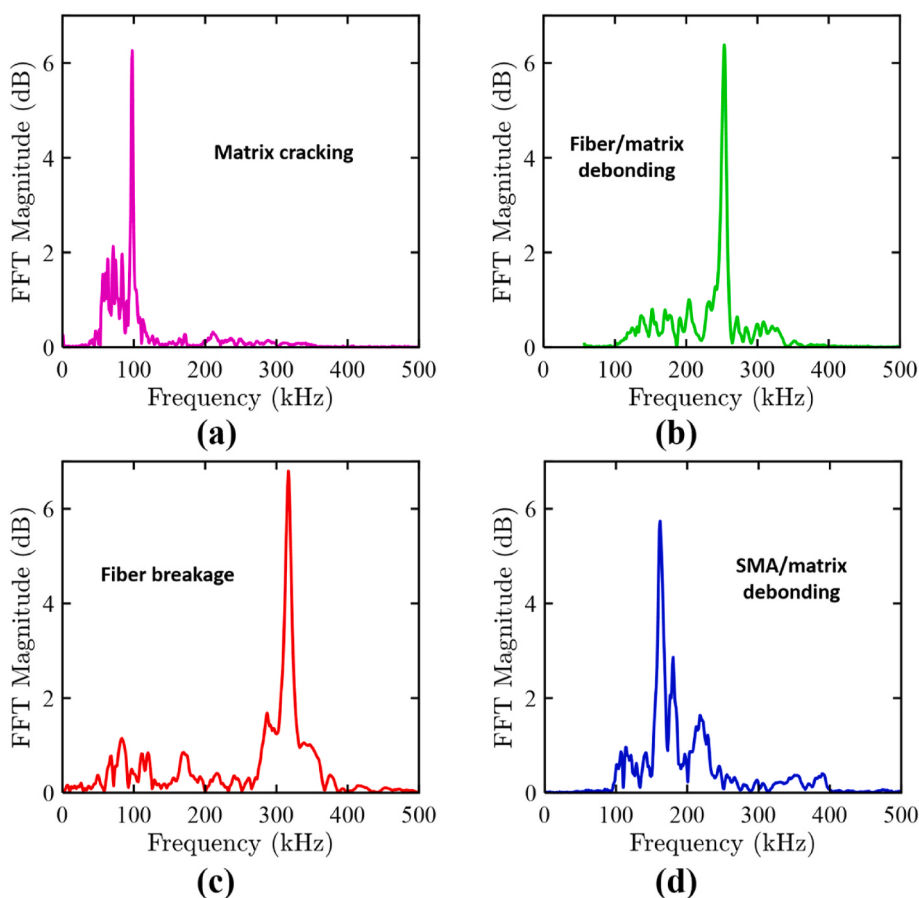


Fig. 7. Frequency domain signals for (a) matrix cracking, (b) fiber/matrix debonding, (c) fiber breakage and (d) SMA/matrix debonding failure modes.

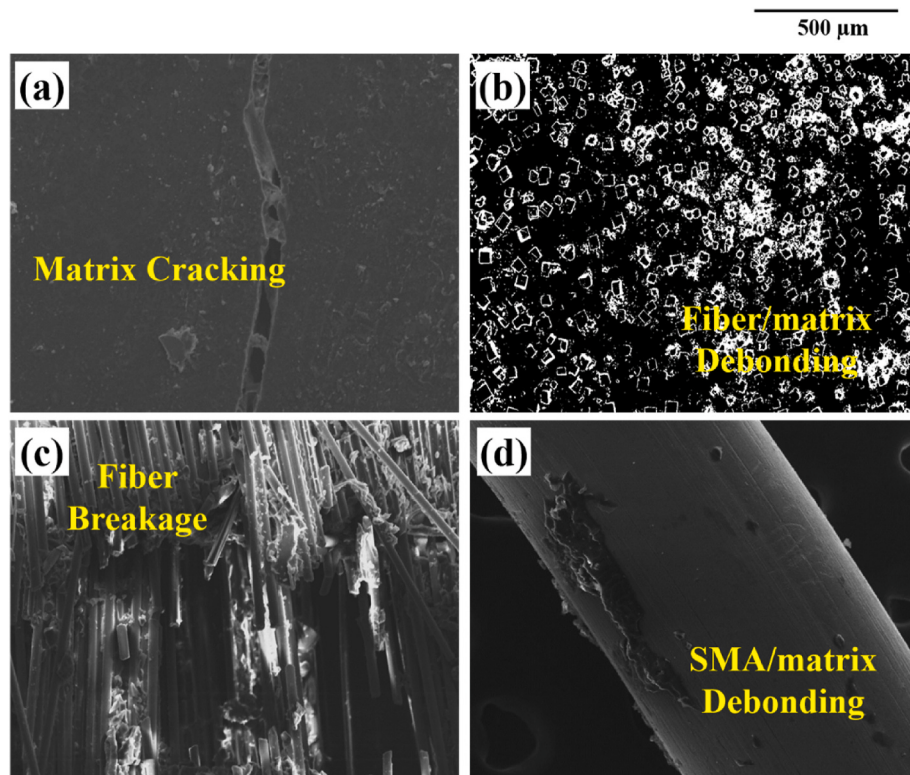


Fig. 8. SEM micrograph of typical (a) matrix cracking, (b) fiber/matrix debonding, (c) fiber breakage and (d) SMA/matrix debonding failure modes.

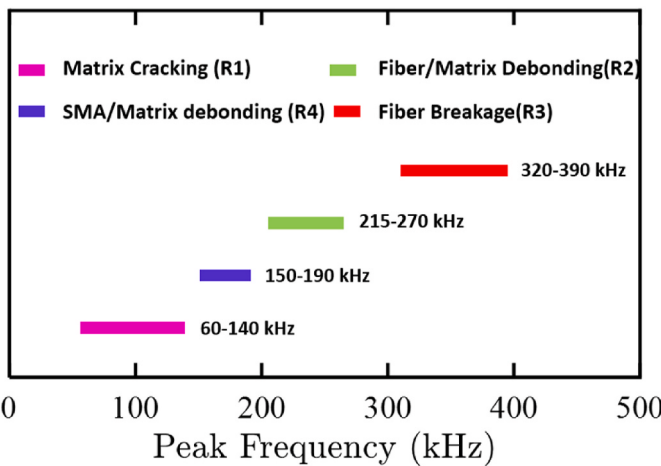


Fig. 9. Peak frequency ranges for different failure modes.

with peak frequency range 60–140 kHz was already identified as a matrix or resin cracking (see Fig. 7 (a)), besides to that when the particulate fibers were soaked to the polymer matrix, there was an increase in the peak frequency range which helped to figure out the frequency range for fiber/matrix debonding. Fig. 7 (b) depicts the distinctive FFT magnitude acquired from particulate glass fiber reinforced epoxy specimens. This FFT plot has a closely identical frequency value as that of range R2. Hence, R2 is obviously associated with fiber/matrix debonding. A typical fiber/matrix debonding on particulate fibers reinforced specimen, as depicted by SEM, is shown in Fig. 8 (b). To identify the cluster related to fiber failure, continuous glass fibers reinforced epoxy specimens were subjected to the indentation test and the predominantly recorded AE events were analyzed. Here, the possible damage modes are resin cracking, fiber/matrix debonding, and fiber fracture [44]. Three dominant frequency ranges were acquired during the test. Two of these peak frequency ranges; namely 60–140 kHz and 210–270 kHz, were already identified as resin cracking and fiber/matrix debonding, respectively. The remaining AE events were in the range of 290–400 kHz. Fig. 7 (c) depicts the distinctive FFT magnitude acquired from continuous glass fibers reinforced epoxy specimens. This FFT plot has similar characteristics as that of range R3 (Fig. 6 (a)). Hence, the AE events under R3 are allied with fiber breakage. A typical fiber fracture of continuous glass fibers reinforced specimen, as depicted by SEM, is shown in Fig. 8 (c). SE-SMA/epoxy specimens were employed to identify the AE events allied with SMA/matrix pull-out. The possible damage

modes allied with SE-SMA/epoxy specimens were resin cracking and SMA/matrix pull-out. In addition to AE events associated with matrix cracking, there was yet another distinctive frequency content observed during the testing from SE-SMA based specimens (Fig. 7 (d)). This FFT plot has closely identical dominant frequency content as that of range R4 (150–190 kHz) (Fig. 6 (b)). Hence, R4 is obviously associated with SMA/matrix pull-out [29]. A typical SE-SMA/matrix pull-out, as depicted by SEM, is shown in Fig. 8 (d). Peak frequency ranges associated with various failure modes are illustrated in Fig. 9.

3.3. Correlation of indentation test and AE test results

The stiffness and residual displacement of different glass/epoxy specimens at different indentation cycles are illustrated in Fig. 10. After each indentation cycle, specimens were removed from the fixture, and photographic images of the rear side of the specimens were captured and depicted in Fig. 11. The experimental curves are correlated with the location of different failure modes, and AE cumulative counts for different specimens at various indentation cycles in Fig. 12. At the 1st indentation cycle (i.e. maximum displacement = 2 mm), the Type I specimens depicted the highest linear stiffness and the lowest permanent displacement. These results are ascribed to the brittle and low strain to failure properties of the glass fibers [46–48]. In contrast, Type IV specimens showed the highest permanent deflection and the least stiffness, highlighting that it tolerated the applied indentation in a ductile way with higher deflection owing to the high elongation property of SE-SMA wire. The other SE-SMA based specimens showed a response between Type I and Type IV specimens. In particular, based on the indentation behavior, different glass/epoxy specimens can be ordered from the lower to the higher rank in the following order: Type IV < Type III < Type II < Type I: it is made clear that raising the proportion of SE-SMA on the glass/epoxy composite decreased the linear stiffness of the specimens and induced them to tolerate the out-of-plane indentation load in a ductile manner. The trend of residual deformation is the converse to the stiffness. At higher indentation cycles, the Type I and different SE-SMA reinforced specimens showed an extremely dissimilar response to the indentation load. The indentation behavior tends to be progressively dependent on the SE-SMA architecture at higher cycles, and the rankings changed in comparison to initial ones. This underlines that with the increase in indenter displacement, the damage mechanisms accountable for the absorption of indentation energy (i.e. load) were different.

In 2nd indentation cycles, the changes in stiffness were comparable as for the 1st indentation cycle. However, the difference in stiffness

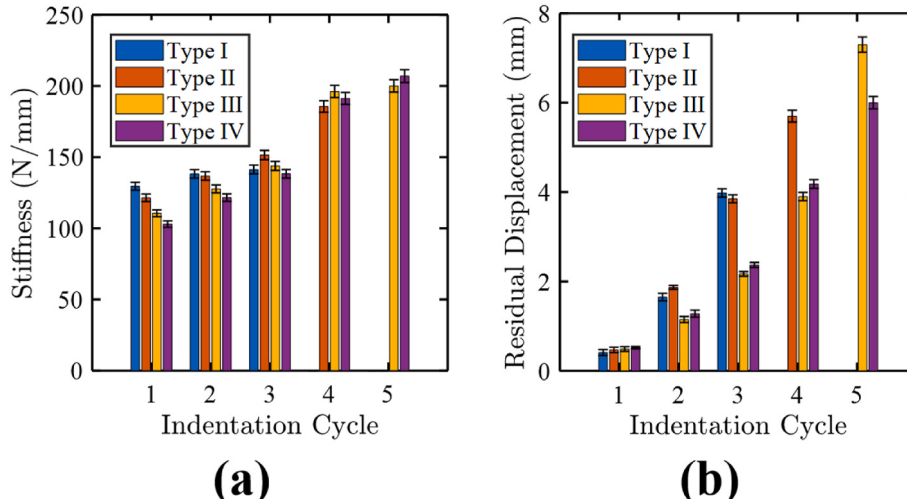


Fig. 10. (a) Stiffness and (b) permanent deformation progression of different glass/epoxy specimens.

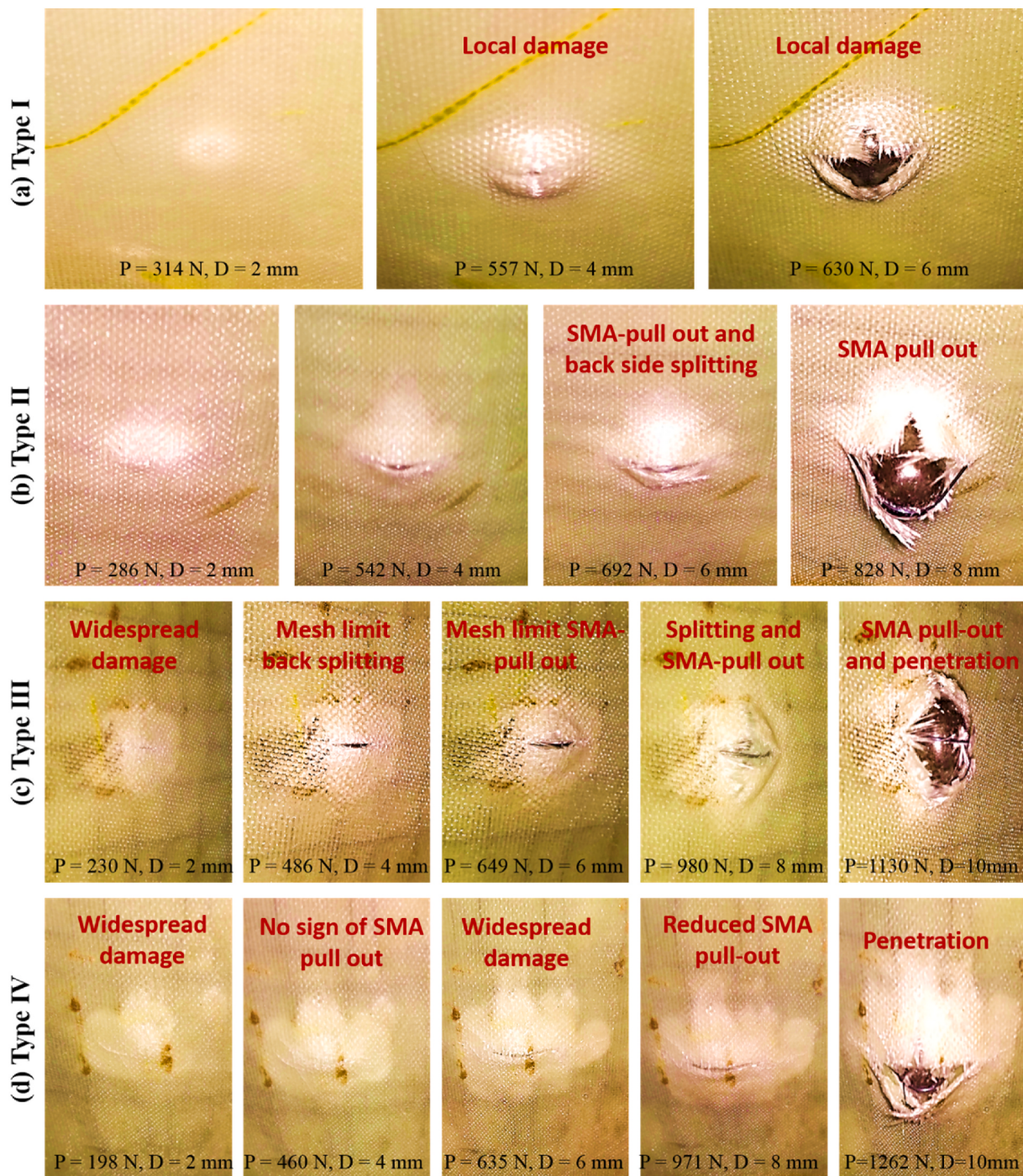


Fig. 11. Photographic images of fractured glass/epoxy specimens at various indentation cycles.

among Type I and SMA based specimens was reduced further than in the previous cycle because the indenter partially penetrated the Type I specimen (Fig. 11 (a)). The trend of stiffness for different specimens in the 3rd indentation cycle was not the same as in the 2nd indentation cycle. At the 3rd indentation cycle, Type I specimens ultimately failed by a sudden drop in load curve after attaining the peak stress. This is due to the brittle nature of the homogeneous glass fibers [49,51]. In Type I specimens, the position of the damaged spot liable for the major AE events was intensively located in and around the midpoint of the specimen (i.e. between -20 mm and 20 mm) (see Fig. 12 (a)), as clearly confirmed by the photographic images in Fig. 11 (a). Moreover, contrary to progressively increasing cumulative counts of SE-SMA based

specimens, in Type I specimen considerable growth in the cumulative counts (w.r.t time) took place from the initial stages of loading itself (see Fig. 12) due to the brittle fracture of glass fibers [41,50]. This critical fiber fracture, largely localized in the middle area, quickly puts off external layers from withstanding tensile stress in the rear side, leading to its ultimate failure.

In the 3rd indentation cycle, the difference in stiffness among Type II and Type III specimens was considerably lower than in previous cycles. The Type II specimens, despite showing superior indentation properties when compared to Type III specimens at earlier cycles, exhibited a critical drop in indentation properties at the 4th cycle (Figs. 4 and 10). At the 4th indentation cycle, Type III specimens surpassed Type II

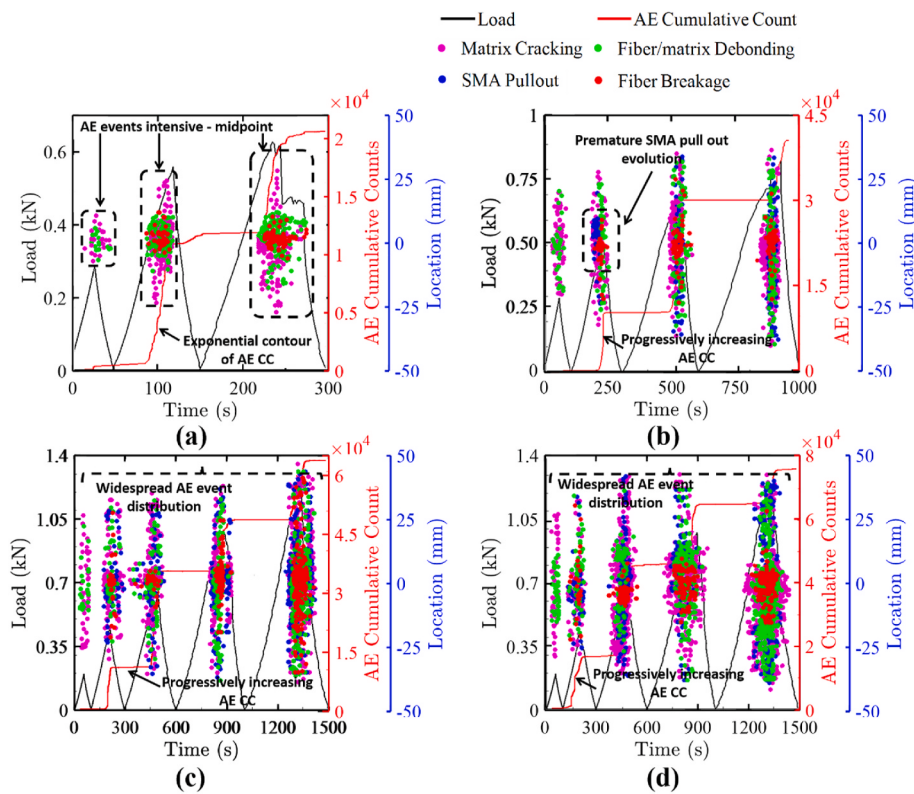


Fig. 12. Indentation load, AE cumulative counts and AE event location versus time for (a) Type I, (b) Type II, (c) Type III and (d) Type IV specimens.

specimens (i.e. in terms of stiffness for the reason that Type II specimens encountered critical rear face fiber breakage with associated SMA/matrix debonding (see Fig. 11 (b)). Also, it can be seen that the Type II specimens showed the ultimate failure at lower displacement than other SE-SMA based specimens (Table 5). For Type II specimens, each wire acted as a separate system. Thus, for better energy absorption wire must be present in the indentation area. The load-carrying capability of this specimen increased until the bond between a particular wire and matrix system was intact. The bonding of other wire which was not directly under the load doesn't play an important role in the energy absorption. As a result, once the SMA/matrix debonding occurred in Type II specimens, it tends to encourage the center fibers to completely withstand the rear side tensile stress, thus resulting in the premature ultimate failure. For meshed configuration (Type III), though maximum energy absorption happened by the wire under the indentation point, because of the presence of mesh, the load was distributed all across the mesh. Thus, other wires which were not directly under indentation load also played a pivotal role in load distribution. This also delayed and reduced the SMA/matrix debonding. Even if, debonding took place at the indentation site, meshed configuration continued to absorb energy through the surrounding wires. From the photographic images, Type II specimen depicted widespread bulge on the tensile or back face (see Fig. 11 (b)) as a result of the high pull-out of the SE-SMA wire and fiber/matrix debonding. Besides, the AE localization plot revealed that the damaged area extended to a wide region, and the SMA/matrix debonding AE events was considerable in a region between -35 mm and +35 mm (Fig. 12 (b)). Critical debonding between SE-SMA wire and matrix system resulted in higher stresses in the rear side fibers and thus leading to premature failure of Type II specimens compared with Type III and Type IV specimens. Furthermore, from AE plots, SMA/matrix pull-out was the critical damage mode in deciding premature ultimate failure of Type II specimens as all the other SMA based specimen's depicted critical SMA wire/matrix debonding at higher indentation load (Fig. 12). These results can describe why the performance of Type II specimens was lower

than that of Type III specimens at the 4th indentation cycle.

Type IV specimens depicted a different behavior, which was characterized by a better indentation response as the SE-SMA architecture pattern largely constrained the failure propagation in between the SMA/matrix interface and at the backside of the specimen from the initial cycle of loading [47]. At higher indentation cycles, Type IV specimens showed an excellent balance among rigidity, rear face fiber breakage, and SMA/matrix pull-out. Consequently, the ultimate deflection to failure was appreciably higher for Type IV specimens rather than other specimens. It can be noted in Fig. 10 (a) and Fig. 10 (b) that the drift of stiffness and residual deflection for Type III and Type IV specimens at the 4th cycle was the same as previous cycles. Nevertheless, in the 4th cycle, the variation in stiffness and permanent deflection among Type III and Type IV specimens was lower than previous cycles. In Type IV specimens, the meshes restricted penetration of indenter and delayed the critical fiber fracture (Fig. 11 (d)) unlike Type I and Type II, whereas the anchors further restricted extensive SMA/matrix pull-out, unlike Type III specimens. This implies that for the ultimate collapse of Type IV specimen, the indentation energy has to be raised more, emphasizing the greater load-carrying capability.

At the 5th cycle, Type IV specimen's surpassed Type III ones (i.e. in terms of peak load, stiffness as Type III ones encountered premature pull-out and fiber fracture (Fig. 11 (c) and 12 (c)). In the case of Type IV specimens, anchors (with knot connection type) further strengthened the GFRP and SE-SMA bond (control the premature pull-out of SE-SMA wires) and hold it in position. The major role of these anchors is to reduce the pull-out lengths while SE-SMA wire undergoes indentation. Thus, for the same indentation displacement, the pull-out length was the least in Type IV configuration. As a result, the entire specimen was perfectly involved in the ultimate fracture process (see Fig. 11 (d)). Among various SE-SMA based specimens, Type IV specimens were the only ones to fail at higher displacement (see Fig. 11) with a display of reduced local elongation of SE-SMA wire. These observations can provide clues on why Type IV specimens showed a superior indentation

response compared to all the other specimens.

The positive role played by the anchors of Type IV specimens on the indentation response is apparent in comparison to other SMA configurations. The results also point out that embedding the SE-SMA wire in Type IV pattern made the progression of premature rear face fiber fracture difficult under indentation loading (greater damage resistance).

4. Conclusions

Cyclic quasi-static indentation tests coupled with AE monitoring were performed to study the indentation response of SE-SMA based composite specimens. The findings of this study would significantly benefit the conventional materials used in aerospace industry. The experimental results observed from the cyclic quasi-static indentation tests as well as detailed AE monitoring leads to the following conclusions:

1. Embedding the glass/epoxy specimens using Type II, Type III and Type IV SE-SMA wires increases the ultimate indentation load-carrying capacity approximately by 31%, 79%, and 100%, respectively, in comparison to the Type I specimens. This could have implications on the safe-fail design of the composite apart from low-velocity impact resistance.
2. Type IV specimens depicted a better indentation response with a regular drop pattern from the initial cycle of loading. At higher indentation cycles, Type IV specimens showed a most excellent balance among rigidity, rear face fiber breakage, and SMA/matrix pull-out.
3. SMA wire/matrix bonding is key to the performance of the composite to make sure the ductility of SMA wire is utilized effectively. Thus, SMA wire/matrix debonding is the vital failure mode governing the ultimate failure of specimens reinforced with SMA wires. Critical debonding between SMA wire and matrix system results in higher stresses in the outermost tensile fibers and thus leading to premature failure of the specimens.
4. In Type III specimens, the meshes restricted penetration of indenter and delayed the critical fiber fracture unlike Type I and Type II, whereas anchored in Type IV specimens further restricted extensive SMA/matrix pull-out, unlike Type III specimens.
5. In Type IV specimens, the load is distributed uniformly all across the anchors. Thus, other wires which are not directly under indentation load also play a pivotal role in load distribution. Moreover, anchors strengthened the GFRP and SMA bond, thus reducing the pull out to the maximum extent for the same indentation displacement in this configuration.

Authors statement

Based on three positive reviews and suggestions, the manuscript is strengthened by the changes we made in response to the reviewer's excellent feedback. Our responses to the first, second and third reviewer's comments are in green, dark red and purple colors, respectively.

Declaration of competing interest

There is no conflict of interest.

Acknowledgements

The authors are immensely grateful to Dr. V. Arumugam, Associate Professor, Department of Aerospace Engineering, MIT Campus, Anna University, Chennai, India for providing Acoustic emission monitoring facility to perform damage evaluation studies.

Appendix A. Supplementary data

Supplementary data to this article can be found online at <https://doi.org/10.1016/j.polymertesting.2020.106942>.

References

- [1] J. Jefferson Andrew, M. Srinivasan Sivakumar, A. Arockiarajan, Hom Nath Dhakal, Parameters influencing the impact response of fiber-reinforced polymer matrix composite materials: a critical review, *Compos. Struct.* 224 (2019) 111007.
- [2] S.W.F. Spronk, Mathias Kersemans, J.C.A. De Baerdemaeker, F.A. Gilabert, R.D. B. Sevenois, D. Garoz, C. Kassapoglou, Wim Van Paepengem, Comparing damage from low-velocity impact and quasi-static indentation in automotive carbon/epoxy and glass/polyamide-6 laminates, *Polym. Test.* 65 (2018) 231–241.
- [3] M.O.W. Richardson, M.J. Wisheart, Review of low-velocity impact properties of composite materials, *Compos. Appl. Sci. Manuf.* 27 (12) (1996) 1123–1131.
- [4] Andrew J. Jefferson, M. Srinivasan Sivakumar, A. Arockiarajan, Effect of multiphase fiber system and stacking sequence on low-velocity impact and residual tensile behavior of glass/epoxy composite laminates, *Polym. Compos.* 40 (4) (2019) 1450–1462.
- [5] R. Bhoominathan, Vellayaraj Arumugam, Ashok Thompson, Jeyakumar Jefferson Andrew, Residual strength estimation of CFRP laminates subjected to impact at different velocities and temperatures, *Polym. Compos.* 38 (10) (2017) 2182–2191.
- [6] S.L. Angioni, M. Meo, A. Foreman, Impact damage resistance and damage suppression properties of shape memory alloys in hybrid composites—a review, *Smart Mater. Struct.* 20 (1) (2010), 013001.
- [7] M. Meo, F. Marulo, M. Guida, S. Russo, Shape memory alloy hybrid composites for improved impact properties for aeronautical applications, *Compos. Struct.* 95 (2013) 756–766.
- [8] B. Han, Y. Wang, S. Dong, L. Zhang, S. Ding, X. Yu, J. Ou, Smart concretes and structures: a review, *J. Intell. Mater. Syst. Struct.* 26 (11) (2015) 1303–1345.
- [9] B. Mas, D. Biggs, I. Vieito, A. Cladera, J. Shaw, F. Martínez-Abella, Superelastic shape memory alloy cables for reinforced concrete applications, *Construct. Build. Mater.* 148 (2017) 307–320.
- [10] Z.G. Wei, R. Sandstrom, S. Miyazaki, Shape memory materials and hybrid composites for smart systems: Part II Shape-memory hybrid composites, *J. Mater. Sci.* 33 (15) (1998) 3763–3783.
- [11] J. Raghavan, T. Bartkiewicz, S. Boyko, M. Kupriyanov, N. Rajapakse, B. Yu, Damping, tensile, and impact properties of superelastic shape memory alloy (SMA) fiber-reinforced polymer composites, *Compos. B Eng.* 41 (3) (2010) 214–222.
- [12] T.C. Kiesling, *Impact Failure Modes of Graphite/Epoxy Composites with Embedded Superelastic Nitinol*, Doctoral dissertation, Virginia Tech, 1995.
- [13] J.S. Paine, C.A. Rogers, *Low Velocity Perforating Impact Response of Shape Memory Alloy Hybrid Composite Materials*, vol. 45, American Society of Mechanical Engineers. Aerospace Division. Publication AD., 1994, pp. 75–84.
- [14] W.B. Cross, A.H. Kariotis, F. Stimler, J. Nitinol Characterization Study, Goodyear Aerospace Corporation, 1970. Report No. GER 14188.
- [15] F.C. Campbell, 1-2, Manufacturing Processes for Advanced Composites, vol. 25, Elsevier, 2004, 61–61.
- [16] C. Shen, Z. Wu, Z. Gao, X. Ma, S. Qiu, Y. Liu, T. Sun, Impact protection behavior of NiTi shape memory alloy wires, *Mater. Sci. Eng., A* 700 (2017) 132–139.
- [17] S. Barberino, E.S. Flores, R.M. Ajaj, I. Dayyani, M.I. Friswell, A review on shape memory alloys with applications to morphing aircraft, *Smart Mater. Struct.* 23 (6) (2014), 063001.
- [18] Wei Wang, Fang Cheng, Liu Jia, Large size superelastic SMA bars: heat treatment strategy, mechanical property and seismic application, *Smart Mater. Struct.* 25 (7) (2016), 075001.
- [19] Cheng Fang, Yue Zheng, Junbai Chen, Michael CH. Yam, Wei Wang, Superelastic NiTi SMA cables: thermal-mechanical behavior, hysteretic modelling and seismic application, *Eng. Struct.* 183 (2019) 533–549.
- [20] J.S. Paine, C.A. Rogers, Improved impact damage resistance in adaptive shape memory alloy hybrid composite materials, in: *Smart Structures and Materials: Smart Structures and Intelligent Systems*, vol. 2190, International Society for Optics and Photonics, 1994, pp. 402–410.
- [21] Z.G. Wei, R. Sandström, S. Miyazaki, Shape-memory materials and hybrid composites for smart systems: Part I Shape-memory materials, *J. Mater. Sci.* 33 (15) (1998) 3743–3762.
- [22] M. Amano, Y. Okabe, N. Takeda, Evaluation of crack suppression effect of TiNi SMA foil embedded in CFRP cross-ply laminates with embedded small-diameter FBG sensor, *JSME International Journal Series A Solid Mechanics and Material Engineering* 48 (4) (2005) 443–450.
- [23] S. Pappadà, R. Rametta, A. Largo, A. Maffezzoli, Low-velocity impact response in composite plates embedding shape memory alloy wires, *Polym. Compos.* 33 (5) (2012) 655–664.
- [24] S. Abrate, *Impact on Composite Structures*, Cambridge University press, 2005.
- [25] J. Jefferson Andrew, V. Arumugam, K. Saravanan Kumar, Hom Nath Dhakal, C. Santulli, Compression after impact strength of repaired GFRP composite laminates under repeated impact loading, *Compos. Struct.* 133 (2015) 911–920.
- [26] Jefferson Andrew, C. Ramesh, Residual strength and damage characterization of unidirectional glass–basalt hybrid/epoxy CAI laminates, *Arabian J. Sci. Eng.* 40 (6) (2015) 1695–1705.

- [27] P. Chen, Z. Shen, J. Xiong, S. Yang, S. Fu, L. Ye, Failure mechanisms of laminated composites subjected to static indentation, *Compos. Struct.* 75 (1–4) (2006) 489–495.
- [28] C. Bouvet, S. Rivallant, J.J. Barrau, Low velocity impact modeling in composite laminates capturing permanent indentation, *Compos. Sci. Technol.* 72 (16) (2012) 1977–1988.
- [29] A. Wagih, P. Maimí, N. Blanco, J. Costa, A quasi-static indentation test to elucidate the sequence of damage events in low velocity impacts on composite laminates, *Compos. Appl. Sci. Manuf.* 82 (2016) 180–189.
- [30] E. Panettieri, D. Fanteria, M. Montemurro, C. Froustey, Low-velocity impact tests on carbon/epoxy composite laminates: a benchmark study, *Compos. B Eng.* 107 (2016) 9–21.
- [31] R. Bogenfeld, J. Kreikemeier, T. Wille, Review and benchmark study on the analysis of low-velocity impact on composite laminates, *Eng. Fail. Anal.* 86 (2018) 72–99.
- [32] K.T. Tan, N. Watanabe, Y. Iwahori, X-ray radiography and micro-computed tomography examination of damage characteristics in stitched composites subjected to impact loading, *Compos. B Eng.* 42 (4) (2011) 874–884.
- [33] P. Gaudenzi, M. Bernabei, E. Dati, G. De Angelis, M. Marrone, L. Lampani, On the evaluation of impact damage on composite materials by comparing different NDI techniques, *Compos. Struct.* 118 (2014) 257–266.
- [34] M.M. Shokrieh, A.G. Mohammadi, Destructive techniques in the measurement of residual stresses in composite materials: an overview, in: *Residual Stresses in Composite Materials*, 2014, pp. 15–57.
- [35] V.I. Rizov, Non-linear indentation behavior of foam core sandwich composite materials—a 2D approach, *Comput. Mater. Sci.* 35 (2) (2006) 107–115.
- [36] Gursahib Singh Bhatia, J. Jefferson Andrew, G. Balaganesan, A. Arockiarajan, The role of patch-parent configurations on the tensile response of patch repaired carbon/epoxy laminates, *Polym. Test.* 70 (2018) 413–425.
- [37] J. Jefferson Andrew, V. Arumugam, Effect of patch hybridization on the compression behavior of patch repaired glass/epoxy composite laminates using acoustic emission monitoring, *Polym. Compos.* 39 (6) (2018) 1922–1935.
- [38] Gursahib Singh Bhatia, J. Jefferson Andrew, A. Arockiarajan, Experimental investigation on compressive behaviour of different patch-parent layup configurations for repaired carbon/epoxy composites, *J. Compos. Mater.* 53 (23) (2019) 3269–3279.
- [39] J.F. Chen, E.V. Morozov, K. Shankar, Simulating progressive failure of composite laminates including in-ply and delamination damage effects, *Compos. Appl. Sci. Manuf.* 61 (2014) 185–200.
- [40] J. Jefferson Andrew, V. Arumugam, C. Ramesh, Acoustic emission characterization of local bending behavior for adhesively bonded hybrid external patch repaired glass/epoxy composite laminates, *Struct. Health Monit.* 18 (3) (2019) 739–756.
- [41] J. Jefferson Andrew, V. Arumugam, D.J. Bull, Hom Nath Dhakal, Residual strength and damage characterization of repaired glass/epoxy composite laminates using AE and DIC, *Compos. Struct.* 152 (2016) 124–139.
- [42] A.J. Jefferson, V. Arumugam, C. Santulli, A. Jennifers, M. Poorani, Failure modes of GFRP after multiple impacts determined by acoustic emission and digital image correlation, *J. Eng. Technol.* 6 (no. 2) (2015) 29–51.
- [43] J. Jefferson Andrew, V. Arumugam, C. Santulli, Effect of post-cure temperature and different reinforcements in adhesive bonded repair for damaged glass/epoxy composites under multiple quasi-static indentation loading, *Compos. Struct.* 143 (2016) 63–74.
- [44] J. Jefferson Andrew, V. Arumugam, C. Ramesh, S. Poorani, C. Santulli, Quasi-static indentation properties of damaged glass/epoxy composite laminates repaired by the application of intra-ply hybrid patches, *Polym. Test.* 61 (2017) 132–145.
- [45] J. Jefferson Andrew, V. Arumugam, Effect of patch hybridization on the tensile behavior of patch repaired glass/epoxy composite laminates using acoustic emission monitoring, *Int. J. Adhesion Adhes.* 74 (2017) 155–166.
- [46] J. Jefferson Andrew, M. Srinivasan Sivakumar, A. Arockiarajan, The role of adhesively bonded super hybrid external patches on the impact and post-impact response of repaired glass/epoxy composite laminates, *Compos. Struct.* 184 (2018) 848–859.
- [47] Luv Verma, Srinivasan M. Sivakumar, Jefferson J. Andrew, G. Balaganesan, A. Arockiarajan, S. Vedantam, Compression after ballistic impact response of pseudoelastic shape memory alloy embedded hybrid unsymmetrical patch repaired glass-fiber reinforced polymer composites, *J. Compos. Mater.* 53 (28–30) (2019) 4225–4247.
- [48] M. Sun, Z. Wang, B. Yang, X. Sun, Experimental investigation of GF/epoxy laminates with different SMAs positions subjected to low-velocity impact, *Compos. Struct.* 171 (2017) 170–184.
- [49] J. Jefferson Andrew, M. Srinivasan Sivakumar, A. Arockiarajan, Influence of patch lay-up configuration and hybridization on low velocity impact and post-impact tensile response of repaired glass fiber reinforced plastic composites, *J. Compos. Mater.* 53 (1) (2019) 3–17.
- [50] M. Saeedifar, M.A. Najafabadi, D. Zarouchas, H.H. Toudehsky, M. Jalalvand, Clustering of interlaminar and intralaminar damages in laminated composites under indentation loading using Acoustic Emission, *Compos. B Eng.* 144 (2018) 206–219.
- [51] C. Ramesh, Joseph Stanley, Vellayaraj Arumugam, Jefferson Andrew, S. Arunabharathi, Effect of multiple impacts on GFRP laminates exposed to hydrolytic ageing using acoustic emission monitoring, *Int. J. Veh. Struct. Syst.* 6 (1/2) (2014) 32.